Ultra-low Energy Phase Change Memory with Improved Thermal Stability by Tailoring the Local Structure through Ag Doping

Soobin Hwang, Hanjin Park, Dasol Kim, Hyeonwook Lim, Changwoo Lee, Jeong Hwa Han, Young-Kyun Kwon, and Mann-Ho Cho*

Read Online

ACCESS | Metrics & More | Article Recommendations | Supporting Information

ABSTRACT: Although Sb_2Te_3, as a candidate material for next-generation memory devices, has attractive properties such as higher operation speed and lower power consumption than $Ge_2Sb_2Te_5$, its poor stability prevents its application to commercial memory devices. Transition metal dopants provide enhancements in its phase change characteristics, improving both thermal stability and operation energy. However, the enhancement mechanism remains to be sufficiently investigated, and standard properties need to be achieved. Herein, the phase change properties of Sb_2Te_3 are confirmed to be enhanced by the incorporation of a heavy transition metal element such as Ag. The crystallization temperature increases by nearly 40%, and the operation energy is reduced by approximately 60%. These enhancements are associated with the changes in the local Sb_2Te_3 structure caused by Ag incorporation. As the incorporated Ag atoms substitute Sb in the Sb−Te octahedron, this turns into a Ag−Te defective tetrahedron with a strong Ag−Te bond that induces distortion in the crystal lattice. The formation of this bond is attributed to the electron configuration of Ag and its fully filled d orbital. Thus, Ag-doped Sb_2Te_3 is a promising candidate for practical phase change memory devices with high stability and high operation speed.

KEYWORDS: phase change materials, Sb_2Te_3, doping, chemical bonding, non-volatile memory, low-energy device
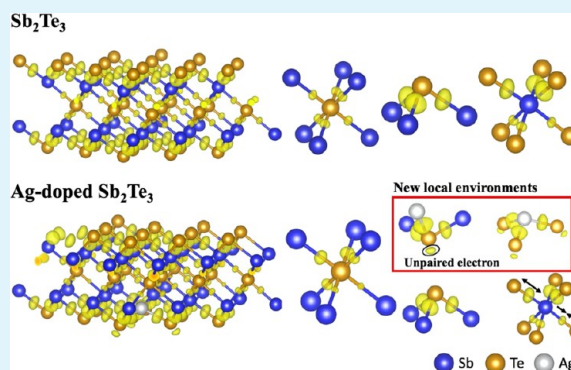
In modern computer architecture for data processing, the memory hierarchy separates computer storage into systematic structures based on response time. Dynamic random-access memory (DRAM) has a relatively high response speed (~10 ns) and volatile properties, whereas flash memory displays a relatively low operation speed (100 μs) and non-volatile properties.[1] Because of their different properties, DRAM and flash memory are commonly used for the main memory and secondary storage, respectively. However, the speed gap between the memory devices poses a bottleneck for data processing; in modern computing systems dealing with a large amount of data, this is a serious issue. To solve this, a novel storage-class memory (SCM)[2] that unifies the main memory and secondary storage has been presented. SCM is expected to be based on non-volatile memory (NVM) devices such as phase change memory, resistance memory, magnetic memory, and ferroelectric memory because these display high speed and nonvolatile properties. The operation mechanism of NVM devices is based on structural changes rather than moving and accumulating electric charge carriers as in traditional Si-based memory devices. However, scaling and a lower operation speed than those of flash memory or DRAM are still issues that prevent the commercialization of NVM devices. Among these, phase change random access memory

(PRAM) is the most promising candidate for SCM because of its low scaling limit (2 nm)[3] and high operation speed (700 ps).[4] Consequently, PRAM is already commercialized as Intel's Optane memory.[5]

Most studies on the commercialization of PRAM devices have focused on $Ge_2Sb_2Te_5$ (GST), a pseudo-binary material made of GeTe and Sb_2Te_3, because of its high stability and reliable operation speed. The phase change mechanism observed in GST is explained with an umbrella flip-flop model, in which the phase change from amorphous to crystalline (with a Peierls-like distortion) is related to a transition from a Ge-centered tetrahedron to an octahedron.[6] The model allows designing the structure of GST locally, including incorporated atoms. In fact, many studies focused on doping to enhance the phase change properties of GST by introducing changes in the tetrahedron or octahedron. It has been reported that dopants such as C[7,8] and N[9] can increase
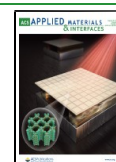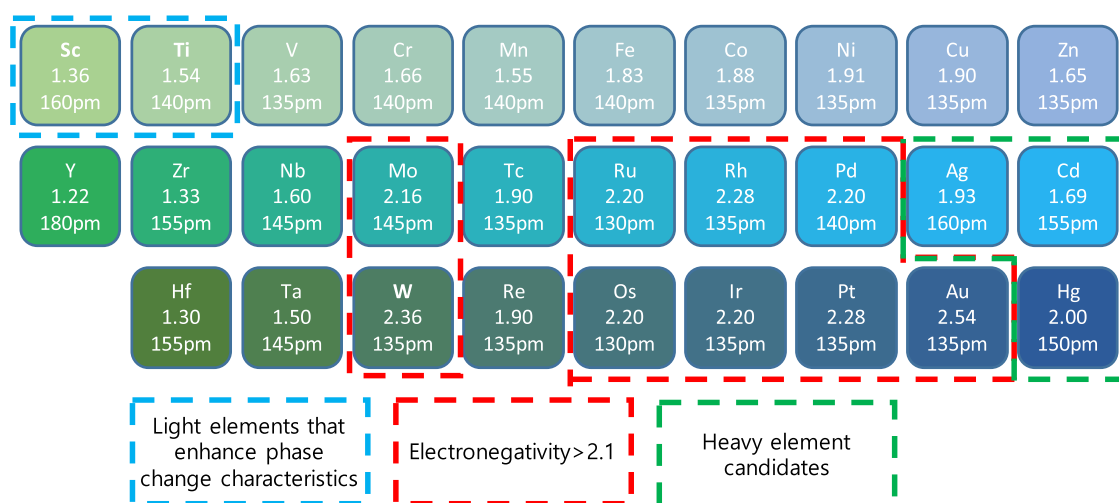
Figure 1. Electronegativity (2nd row of each box) and atomic radius (3rd row of each box) of transition metals. The light dopants that showed remarkable enhancements in the phase change properties of Sb_2Te_3 are marked by a blue dashed box. Elements with a higher electronegativity than that of Te (2.1) are indicated by a red dashed box. These elements may not bond to Te. Heavy transition metals that could enhance the phase change properties of Sb_2Te_3 are indicated by a green dashed box.

the thermal stability and retention time of GST. A binary material such as BN acts as a nucleation center in the crystallization process and improves the operation speed and thermal stability of GST.[10] Although it has been recently reported that a transition metal dopant such as Ag lowers the crystallization temperature of GST, which may induced by an increase in Peierls distortion,[11] remarkable enhancements in the operation speed of GST have not been reported yet. A recently reported superlattice structure of GeTe and Sb_2Te_3 (GT-ST superlattice) showed very attractive information on PRAM performance. The operation mechanism of GT-ST superlattice is based on crystal-to-crystal transition without amorphization. This reduces entropic losses during operation, and therfore very low energy consumption and an exceptional increase in cyclability can be achieved. However, exact operation mechanism of GT-ST superlattice is yet debating and fabricating multiple layers with single crystal is yet challenging.[12]

For a long time, another phase change material (PCM), Sb_2Te_3, has received much attention because of its very fast operation speed, faster than that of GST. Although the fast operaton speed is very attractive to replace GST, the very poor stability of Sb_2Te_3 limits its application in the devices.[13,14] In fact, its low crystallization temperature (∼100 °C) can result in an amorphous-to-crystalline phase change during device operation, which is a critical issue for the development of real devices. To overcome this issue, dopants such as N,[15] O,[16] Al,[17] and V[18] have been investigated in many studies. Although the thermal stability and crystallization temperature increased, most dopants cause the deterioration of other phase change properties, such as the ON−OFF ratio, cyclability, and even operation speed. In particular, higher thermal stability may conclude to an increase in operation speed or operation energy. An increase in thermal stability means a more stable amorphous structure; therefore, SET-to-RESET operation may need more energy. Recently, transition metal dopants provided notable stability and efficiency with introducing proper distortion in the Sb_2Te_3 crystal lattice. Unlike other elements, transition metals display a unique valence-shell electron configuration. Because the energy level of the $(n − 1)$ d

orbital in the valence shell is comparable to that of the n s orbital, the former can be filled partially while filling the latter. This affects the bonding properties in transition metal compounds. In Ti-doped Sb_2Te_3, strong covalent interaction between the Ti-3d orbital and Te-5p orbital yields a local Ti_2Te octahedral structure with six identical strong bonds.[19] This, in turn, distorts the local structure of Sb_2Te_3, causing comparable thermal stability and one order of magnitude faster operation speed with respect to GST. In Sc-doped Sb_2Te_3, the generation of a robust Sc−Te bond in the local Sc_2Te_3 structure reduces the stochasticity of crystal nucleation, resulting in subnanosecond operation speeds.[4] It is remarkable that both Sc and Ti substitute Sb in Sb_2Te_3, forming a strong bond with Te. Another effect that originates from the unique properties of the d orbital is the d-block contraction.[20] As the atomic number increases, the nucleus attracts valence electrons more strongly. However, because the electron density of the d orbital is lower than that of the s or p orbital, the shielding of the nuclear charge in the d orbital is weaker, and the effective nuclear charge becomes larger than its theoretical value. As a result, transition metals display a smaller atomic radius than the calculated one, whereas post-transition metals, which have a fully filled d orbital and s or p orbitals affecting the valence state, have an atomic radius similar to the calculated one. Thus, heavy transition metals with fully filled d orbitals can affect very differently the phase change properties of Sb_2Te_3 compared with light elements such as Sc and Ti.

The transition metals with their electronegativity and atomic radius are shown in Figure 1. Among the heavy transition metals of the 4th and 5th period, we chose elements with a lower electronegativity than Te (2.1).[21] As an electron acceptor, Te receives electrons from other elements, which can critically affect their chemical bonding. Thus, bonding between Te and an element with a higher electronegativity than Te should not be formed. From the remaining elements, we selected three candidates that have a fully filled d orbital: Ag, Cd, and Hg. Among these, Ag is the most attractive candidate because of its atomic radius. The atomic radius of Ag is the largest (160 pm) among the three elements (Cd: 155 pm, Hg: 150 pm) and larger than that of most light transition
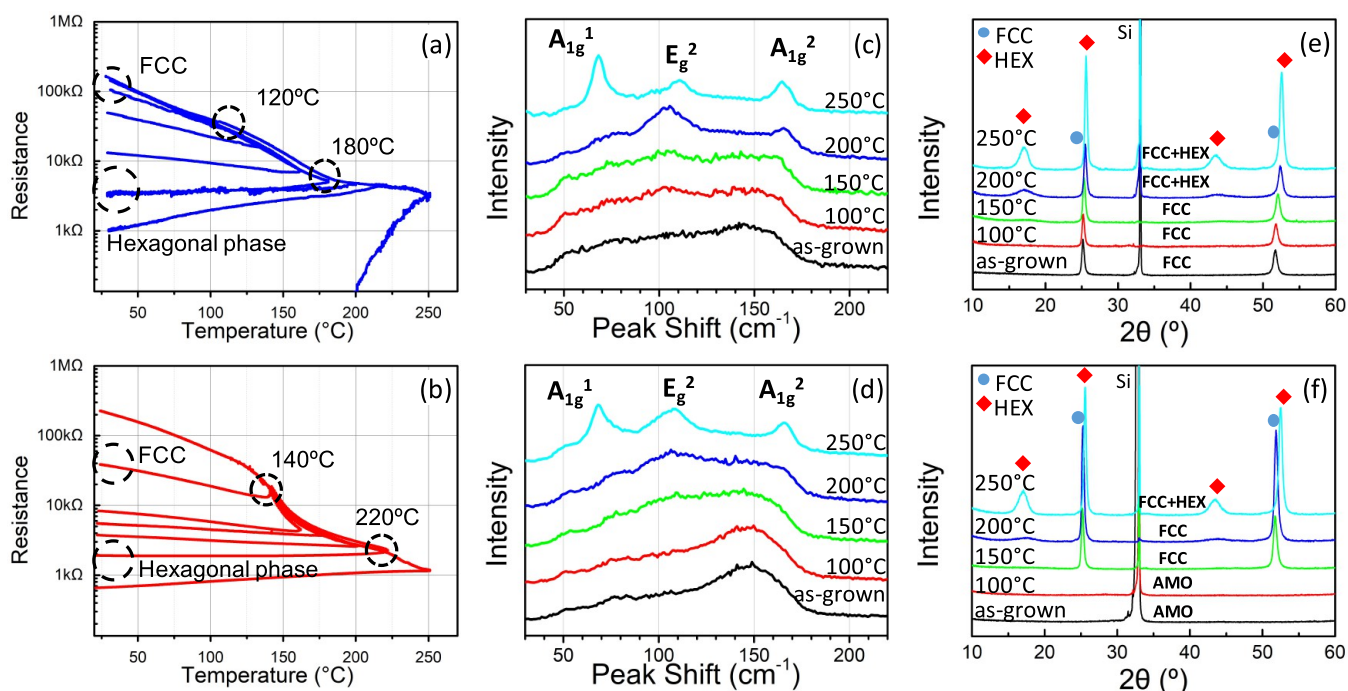
Figure 2. (a, b) Sheet resistance as a function of the annealing temperature of 100 nm-thick (a) Sb_2Te_3 and (b) Ag-doped Sb_2Te_3, with a ramping rate of 10 °C min^{-1}. In (a), the resistance increases upon cooling from above 120 °C, which is attributed to FCC phase arousal and decreases further after heating above 180 °C, which is attributed to hexagonal phase arousal. In (b), the Ag-doped Sb_2Te_3 film displays an FCC phase above 140 °C and hexagonal phase above 220 °C. (c, d) Raman spectra of annealed (c) Sb_2Te_3 and (d) Ag-doped Sb_2Te_3, showing hexagonal phase emergence at 200 °C in Sb_2Te_3 and at 220 °C in Ag-doped Sb_2Te_3. (e, f) XRD data of annealed (e) Sb_2Te_3 and (f) Ag-doped Sb_2Te_3, showing the existence of the FCC phase in the as-grown Sb_2Te_3 film only and hexagonal phase arousal at 200 and 250 °C, respectively.

metals.[22] This indicates that the effective nuclear charge of Ag is weaker than that of other transition metals, and the valence electron of Ag may escape far enough to induce ionic properties in the bond between Ag and Te to some extent. The electronegativity difference with Te is smaller for Ag (0.17) than for Ti (0.56). Thus, the Ag−Te bond is expected to be significantly weaker than the Ti−Te bond. However, the Ag-4d orbital and Te-5p orbital form a strong covalent bond (2.82 Å) in Ag_2Te,[23] which is very similar to the strong covalent bond (~2.77 Å) in $TiTe_2$.[24] Additionally, a recent study on AgInSbTe showed that the bond between Ag and Te is closer to ionic than covalent bonding.[25]

In this study, we investigated the stability, operation speed, and operation energy of Ag-doped Sb_2Te_3. We found that the crystallization temperature of the transition from the amorphous to the FCC crystalline phase increases to 140 °C, and that of the transition from the FCC to the hexagonal phase increases to 220 °C. The SET operation speed is maintained at the same level as Sb_2Te_3, and the RESET energy is lower than that of not only Sb_2Te_3 but even GST and Ti-doped Sb_2Te_3. The local substitution of Ag for Sb in the structure of Sb_2Te_3 is confirmed by experimental data and *ab initio* calculations and is believed to induce a reproducible distortion in the atomic structure of Sb_2Te_3 without structural breakage. Thus, Ag stabilizes Sb_2Te_3 and increases its efficiency. The results of this study indicate transition metal-doped Sb_2Te_3 as the most promising candidate for next-generation PRAM devices.

Ag-doped Sb_2Te_3 films with different dopant concentrations were grown on a Si(100) substrate by ion-beam sputtering deposition (IBSD), co-sputtering the Ag and Sb_2Te_3 targets to find optimal amounts of the dopant. As shown in Figure 2 and

Figure S1, only the film with a Ag concentration of 3.3% showed a stable hexagonal phase until 250 °C. Therefore, we chose 3.3% as the optimal Ag concentration. Sputtering was performed at room temperature under a vacuum pressure of 3 × 10^{-8} Torr. The composition of the 100 nm-thick films obtained was verified to be consistent with the nominal composition by X-ray photoelectron spectroscopy (XPS). In order to determine their crystallization temperature, the resistance of a $Ag_{0.17}Sb_{1.83}Te_3$ and Sb_2Te_3 film was monitored during heating the samples at a ramping rate of 10 °C min^{-1} using a microprobe station. Simultaneously, the sheet resistance was measured by a two-point contact method using a Keithley 2400 sourcemeter. Using the obtained resistance−temperature characteristics, Raman and X-ray diffraction (XRD) spectra were acquired at specific temperatures to confirm the structural changes through the phase change process. The Raman spectra were acquired using a LabRam Aramis Raman spectrometer (Horiba Jovin-Yvon) with a 532 nm Nd:YAG laser light as the excitation source and a 100× microscope objective lens to collect the Raman-scattered light signal. To avoid damaging the samples, the power of the probing laser was maintained below 0.5 mW. The XRD spectra were measured using a high-resolution X-ray diffractometer with a 9 kW Cu Kα radiation source (Rigaku SmartLab). To monitor changes in the Sb, Te, and Ag bonds and confirm the distortions in the Sb_2Te_3 structure caused by Ag doping, XPS was conducted with a monochromatic X-ray source (Al Kα). In Sb_2Te_3 films, Sb can rapidly oxidize to Sb−O,[26] which prevents a correct analysis of the local structure; therefore, exposure to air was avoided using a vacuum transport system. Additionally, an Au film was used to correct unexpected chemical peak shifts caused by charging the

sample. A T-shaped test cell was fabricated to investigate the electrical phase change properties of the Sb_2Te_3 and Ag-doped Sb_2Te_3 films. TiN films of 320 nm in diameter were patterned by photolithography on a Si substrate to form bottom electrode contacts (BEC). A 30 nm-thick (Ag-doped) Sb_2Te_3 film and 50 nm-thick TiN electrode were deposited over the patterns by ion-beam sputtering and radio frequency (RF) sputtering, respectively. To probe the operation of the test cells, an Agilent 33600A pulse generator and Keithley 2636B sourcemeter were used for applying electrical pulses and measuring the resistance during the switching process, respectively. To switch the state of the test cells between SET and RESET, electrical pulses of width 10−200 ns and height 0.05−4 V were applied, and the resistance of the states was measured with a 0.1 V probing voltage. The resistance drift properties of Sb_2Te_3 and Ag-doped Sb_2Te_3 were also investigated using the T-shaped test cell to verify the endurance of these phase change materials (PCMs). The resistance of the cells was measured at a fixed voltage of 0.05 V and at room temperature to exclude external heat effects on the drift properties.[27] To investigate the structural stability and the electronic properties of Ag-doped Sb_2Te_3, we performed density functional theory (DFT)[28] calculations. The primitive unit cell of Sb_2Te_3 is composed of three quintuple layers with $R\overline{3}m$ symmetry and lattice constants $a = b = 4.28$ Å and $c = 30.67$ Å. To find the most favorable Ag site in the Sb_2Te_3 crystal, we substituted a Ag atom for either Sb or Te or added it in the $3 \times 3 \times 1$ supercell of Sb_2Te_3, containing 54 Sb and 81 Te atoms, which is large enough for the Ag atom not to interact with itself in neighboring cells. To find the equilibrium structure of each Ag-doped configuration, we carried out geometrical relaxation while adjusting parameter c and maintaining the $R\overline{3}m$ symmetry with lattice parameters $a = b = 12.79$ Å. The calculated c values were varied in the 30.57−30.89 Å range depending on the locations of the Ag dopant. For the DFT calculation, we expanded the electronic wavefunctions with a planewave basis using a cutoff energy of 400 eV and described the ion−electron interactions through the projector augmented-wave pseudopotentials[29] implemented in the Vienna ab initio simulation package (VASP).[30,31] The exchange-correlation functional was treated within the generalized gradient approximation (GGA) method in the Perdew−Burke−Ernzerhof (PBE) form.[32] The charge density was determined self-consistently with a total energy precision lower than 10^{-5} eV cell^{-1}. Atomic relaxation was continued until the Helmann−Feynman forces acting on every atom became lower than 0.01 eV Å^{-1}. The Brillouin zone corresponding to the $3 \times 3 \times 1$ supercell was sampled using a Γ-centered $2 \times 2 \times 1$ k-grid mesh. To describe accurately the interaction between layers, we included the van der Waals interaction using the DFT-D2 method proposed by Grimme.[33] To explore the local structural properties of Ag-doped Sb_2Te_3, we performed a constant-temperature molecular dynamics (MD) simulation. The quantum mechanical force calculated through the Hellmann−Feynman theorem was applied to solve the classical equation of motion. The constant temperature was maintained by the Nosé thermostat[34−37] with the heat bath temperature set to 300 K. The positions and velocities of every atom, gathered through the 3 ps MD calculation, were used to examine the local environment such as radial distribution functions (RDFs) and angular distribution functions (ADFs).[38]

To compare the relative stability of different Ag-doped Sb_2Te_3 configurations, we considered different substitutional and interstitial sites. Among the substitutional sites, there were only three inequivalent ones, two Te-substitutional and one Sb-substitutional, because of the symmetry. Because the number of atoms of each species differs case by case (substitutional or interstitial), we calculated the formation energy for each configuration, defined as

$$E_f = E_{sys} - E_P - \mu_{Ag} + \mu_M \ (M = Sb, Te)$$

where E_{sys} is the total energy of the Ag-doped Sb_2Te_3 system and E_P is the total energy of the pristine $3 \times 3 \times 1$ Sb_2Te_3 supercell. μ_{Ag} and μ_M are the chemical potentials of the Ag and M (Sb or Te) atoms, respectively. The former was set to the per-atom energy of bulk Ag, and the latter was determined from $E_P = 2n\mu_{Sb} + 3n\mu_{Te}$ with $n = 27$. For the interstitially doped systems, μ_M was set to zero.

The sheet resistance of the Sb_2Te_3 and Ag-doped Sb_2Te_3 films was measured as a function of the annealing temperature ($R-T$ curve), as shown in Figure 2a,d. The data clearly show that the films changed from a semiconducting to metallic phase as the annealing temperature increased. The resistance first decreases with increasing annealing temperature, indicating a semiconducting phase, changing to the opposite behavior (increasing with increasing annealing temperature) because of the transition to the metallic phase. The data reflect the evolution of the crystalline Sb_2Te_3 phase with increasing temperature from the amorphous phase with insulating properties to the crystalline FCC phase with semiconducting properties to the metallic hexagonal phase.[15,39,40] At an annealing temperature of 120 °C, the resistance dropped, and a semiconducting behavior was observed. The Sb_2Te_3 film maintained its semiconducting properties up to 160 °C, and the transition from the semiconducting to the metallic phase appeared clearly at 180 °C. The gradient of the resistance continuously increased with the annealing temperature, which indicates a dominant generation of the metallic phase in crystalline Sb_2Te_3. Failure was eventually observed in the $R-T$ characteristics only in pure Sb_2Te_3 over 250 °C, indicating poor thermal stability. In contrast, the Ag-doped Sb_2Te_3 film showed more robust thermal stability. On the other hand, there was no resistance change in the Ag-doped Sb_2Te_3 film up to an annealing temperature of 120 °C, indicating that the amorphous phase was maintained. The resistance drop around 120 °C was caused by the generation of the semiconducting phase, which was maintained stably until the annealing temperature reached 200 °C. Over 220 °C, the gradient of the resistance became positive because of the onset of the transition to the metallic phase in Ag-doped Sb_2Te_3. The gradual increase in the gradient up to 250 °C, caused by the gradual transition to the metallic phase, displays no signs of failure, indicating a significantly improved thermal stability in Ag-doped Sb_2Te_3. Because of partial crystallization caused by the poor thermal stability in as-grown Sb_2Te_3,[15] there was no abrupt decrease in resistance in the Sb_2Te_3 system, and the crystallization temperature (T_c) cannot be determined exactly. However, the room-temperature resistance difference between the as-grown and annealed film can provide an indication. The resistance of Sb_2Te_3 did not return to its initial state after annealing over 120 °C, which might be a result of crystallization. Similarly, the Ag-doped Sb_2Te_3 showed a resistance difference after annealing over 140 °C, which is a
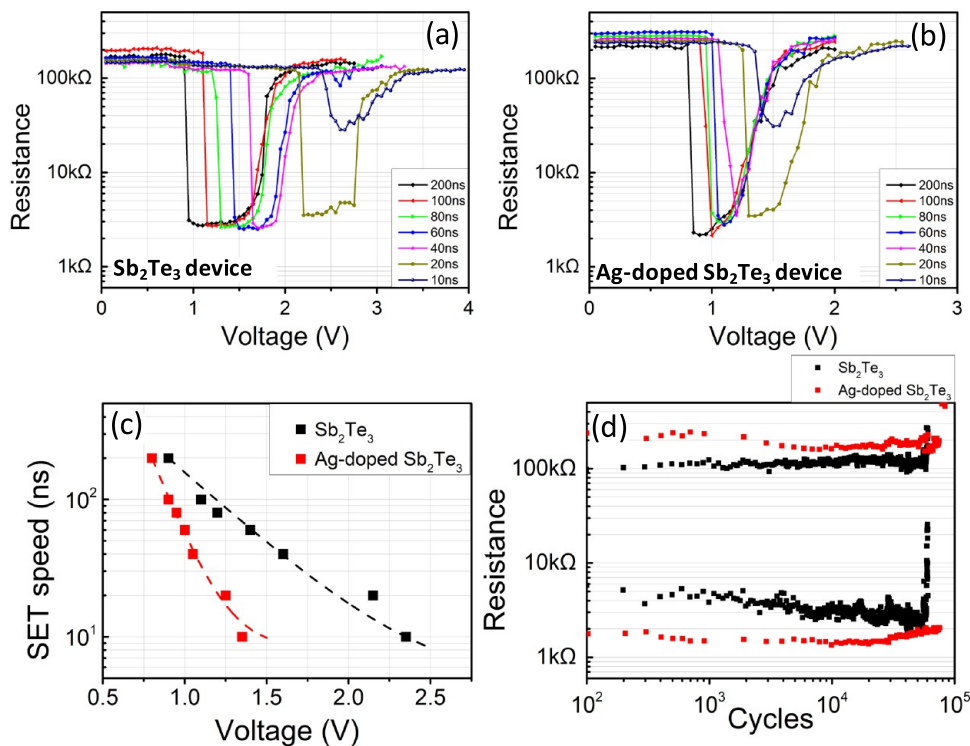
Figure 3. (a, b) Operation characteristics of the PCM test cell for (a) Sb_2Te_3 and (b) Ag-doped Sb_2Te_3. (c) SET operation speed as a function of the applied voltage for Sb_2Te_3 and Ag-doped Sb_2Te_3. (d) Device operation cycles of Sb_2Te_3 and Ag-doped Sb_2Te_3. The SET and RESET states were achieved by applying electrical pulses of width (height) 200 ns (1.3 V) and 60 ns (2 V), respectively. Each operation was maintained for 5.8×10^4 cycles in Sb_2Te_3 and for 8.0×10^4 cycles in Ag-doped Sb_2Te_3.

strong evidence that the T_c of Sb_2Te_3 increases with Ag incorporation. Moreover, the temperature range in which the FCC phase was maintained dramatically increased in Ag-doped Sb_2Te_3, indicating that retention can improve with Ag doping. However, the T_c found from measuring the in-plane resistance may not reflect the crystallization point exactly because the latter depends on the ratio between the crystal and amorphous phases. In addition, data retention is another key factor in the thermal stability of PCM, which shows how long the PCM can maintain stored data at a specific temperature.[41] In Figure S2, data retention of GST, Sb_2Te_3, and Ag-doped Sb_2Te_3 is shown. The temperature for 10 year retention of Ag-doped Sb_2Te_3 is 126 °C, which means the PCM memory cell based on Ag-doped Sb_2Te_3 can maintain its data for 10 years even at 126 °C. The obtained higher value, compared with those of Sb_2Te_3 and GST, indicates that the thermal stability of Ag-doped Sb_2Te_3 is greatly improved.

To determine the exact crystallization and FCC-to-hexagonal phase transition temperature, the crystalline structures of Sb_2Te_3 and Ag-doped Sb_2Te_3 were inspected by Raman spectroscopy for mid-range ordering and X-ray diffraction (XRD) for long-range ordering. Figure 2c,d shows the Raman spectra of Sb_2Te_3 and Ag-doped Sb_2Te_3 as a function of the annealing temperature. Three vibrational modes, A_{1g}^1, E_g^2, and A_{1g}^2, can be observed in hexagonal-phase Sb_2Te_3 at 69, 112, and 166 cm^{-1}, respectively.[42] Instead, the as-grown film with the amorphous phase and annealed film with the FCC phase should display a broad spectrum with no clear peak. It is expected that the spectrum of the FCC phase would extend from 50 to 180 cm^{-1}, and that of the amorphous phase would show its characteristic broad peak arising near 149 cm^{-1}. The observed Raman spectra of the as-grown films of

both Sb_2Te_3 and Ag-doped Sb_2Te_3 show no peaks related to the characteristic vibrational mode. The spectral shape of the as-grown Sb_2Te_3 film is rather similar to that of the FCC phase because of partial crystallization during film growth, whereas the as-grown Ag-doped Sb_2Te_3 one shows a broad but apparent peak near 149 cm^{-1}, implying the structural stability of its amorphous phase. After increasing the annealing temperature to 200 °C, three vibrational modes arise in Sb_2Te_3 and sharpen at 250 °C, indicating the appearance of the hexagonal phase. However, in Ag-doped Sb_2Te_3, the FCC phase is maintained up to 200 °C after appearing at 150 °C, and the hexagonal phase appears only at 250 °C. The crystalline structures of the Sb_2Te_3 and Ag-doped Sb_2Te_3 films were also investigated by XRD as a function of the annealing temperature (Figure 2e,f). The diffraction peaks of the as-grown Sb_2Te_3 film are caused by the FCC phase, corresponding to the (111) and (222) planes of the FCC structure.[15] As the annealing temperature increases, different peaks appear; above 200 °C, the peaks corresponding to the (006), (009), (0015), and (0018) planes of the hexagonal phase of Sb_2Te_3 emerge.[15] In contrast, the peaks of the FCC phase were not observed in the as-grown Ag-doped Sb_2Te_3 film. It seems that the FCC phase begins to form above 100 °C and continues to grow until 200 °C. In this temperature range, its hexagonal phase was not observed but done only over the annealing temperature of 250 °C. Our high-resolution transmission electron microscopy (HR-TEM) images support this evolution of the crystal structure of Sb_2Te_3 and Ag-doped Sb_2Te_3. As shown in Figure S3, the 140 °C-annealed Sb_2Te_3 film and Ag-doped Sb_2Te_3 films display grains in the FCC phase. The 200 °C-annealed Sb_2Te_3 and 220 °C-annealed Ag-doped Sb_2Te_3 films display the van der Waals gap of the
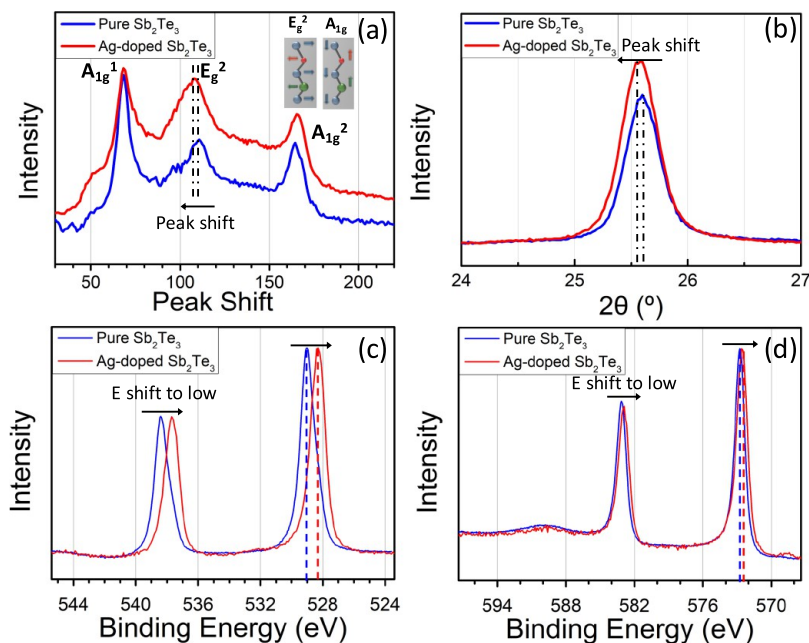
Figure 4. (a) Raman spectra, (b) XRD, and XPS (c) Sb 3d and (d) Te 3d spectra, showing changes in the local structure of Sb_2Te_3 after the Ag incorporation and confirming substitution of Ag in Sb_2Te_3. (a) The peak shift in the Raman spectrum shows the change in the Sb_2Te_3 plane induced by Ag incorporation. (b) The XRD data also verify an increase in the lattice parameter, indicating the substitution of Ag in the Sb_2Te_3 lattice. (c, d) The XPS profiles show that the Sb site is substituted by Ag.

hexagonal phase, and the corresponding selected-area electron diffraction (SAED)[43] patterns confirm a hexagonal structure. Thus, the sheet resistance evolution, Raman spectroscopy, XRD, and HR-TEM data consistently support the enhancement of the thermal stability caused by Ag incorporation into the Sb_2Te_3 film. The crystallization and FCC-to-hexagonal phase transition temperatures of Sb_2Te_3 increase from 100 to 140 °C and from 180 to 220 °C, respectively, with Ag incorporation. In addition, any sign of phase separation between Ag and Sb_2Te_3, such as the formation of Ag cluster or Ag-based compounds of $AgSbTe_2$, Ag_5Te_3, and Ag_2Te phases, is not observed because the amount of Ag incorporated into Sb_2Te_3 is controlled to a low level ($\sim$3.3%). The solubility of Ag to Sb–Te binary compound is dependent on the phase of the compound, i.e., the solubility of Sb_2Te_3 is relatively low compared with that of γ and δ phases.[44] Therefore, we adjust the amount of Ag to a low level to avoid phase separation, thereby achieving good data retention and endurance in device operation.

To evaluate the device performance of Sb_2Te_3 and Ag-doped Sb_2Te_3, the resistance was monitored in T-shaped test cells while applying electrical pulses. The diameter of the bottom electrode was 320 nm, and the width of the pulse was modulated from 10 to 200 ns. The resistance–voltage characteristics for different electrical pulses are shown in Figure 3a,b for Sb_2Te_3 and Ag-doped Sb_2Te_3, respectively. Because a higher pulse is needed for faster operation, in Sb_2Te_3, 0.9–2.35 V pulses for the SET operation and 1.35–2.9 V pulses for the RESET one were needed, changing their width from 200 to 10 ns. Interestingly, the operation voltage could be decreased in Ag-doped Sb_2Te_3 with respect to that of pure Sb_2Te_3: 0.8–1.35 V pulses were needed for the SET operation and 0.95–1.55 V for the RESET operation, with identical pulse width. Moreover, the ON/OFF ratio improved because the amorphous phase was well maintained in the RESET state. To evaluate the performance of Sb_2Te_3 with Ag doping accurately,

the SET operation speed as a function of the SET voltage was investigated (Figure 3c) for a bottom electrode contact (BEC) diameter of 320 nm. Not only was the SET operation speed of Sb_2Te_3 maintained at 10 ns after Ag incorporation but also the SET operation voltage decreased by approximately 30% in Ag-doped Sb_2Te_3, reducing the SET operation energy from 0.84 to 0.34 pJ. Where the SET operation characteristic is a key feature for evaluating the performance in device operation, RESET operation energy is also significant for low power consumption. Particularly, a higher energy for the RESET than for the SET operation can be a bottleneck for the performance of PRAM devices.[45−47] After Ag doping, the RESET energy of Sb_2Te_3 is reduced from 0.15 to 0.05 nJ. Furthermore, this is about three orders of magnitude lower than that of the GST device with more scaled BEC.[19] Considering that scaling the diameter of BEC makes the operation energy lower, the Ag-doped Sb_2Te_3 device with identical BEC to the GST should show a much lower energy than studied in this work. To calculate the SET (E_{SET}) and RESET (E_{RESET}) operation energies, we used the equation $E_i = (V_i^2 \times t_i)/R_i$, where V_i and t_i are the height and width of the pulse, respectively, and R_i is the resistance of the i = SET, RESET operation.[15,48,49] In addition to the operation speed and energy, endurance is also an important feature for the commercialization of PCM devices. We, therefore, compared the cyclability properties of Sb_2Te_3 and Ag-doped Sb_2Te_3 (Figure 3d). The switching cycle between the SET and RESET state is improved after the incorporation of Ag: the cyclability of Sb_2Te_3 is 5.8×10^4 cycles, and that of Ag-doped Sb_2Te_3 is 8.0×10^4 cycles. This is even better than the GST with identical device platform, as shown in Figure S4. Additionally, we evaluated the resistance drift coefficients, which are also important characteristics of determining the endurance of the device, of Sb_2Te_3 and Ag-doped Sb_2Te_3 (Figure S5). The increase in resistance with time is approximately 10% lower after Ag incorporation in Sb_2Te_3. By comparing the device operation characteristics of Sb_2Te_3
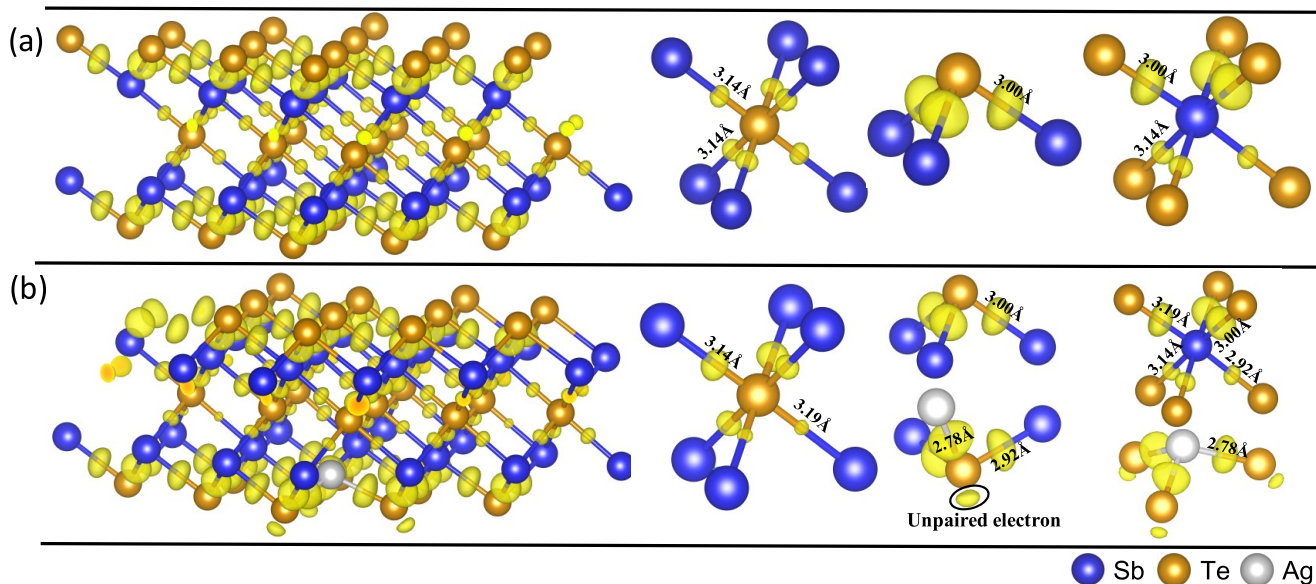
Figure 5. Hexagonal lattices of (a) Sb_2Te_3 and (b) Ag-doped Sb_2Te_3 with their respective CDD. Blue-, gold- and silver-colored balls denote Sb, Te, and Ag atoms, respectively. The bond length cutoff of 3.2 Å was determined from the RDF result shown in Figure S7a. The isosurface value was set to 0.0045 e·a_0^{-3} (a_0 = Bohr radius). The isosurfaces shaded in yellow show the region of clustered electrons, indicating atomic bond formation. The right panels show the local environments of Sb_2Te_3 and Ag-doped Sb_2Te_3. The incorporated Ag substitutes Sb and turns the Sb-centered octahedron into a defective tetrahedron. The short and long bonds of the Sb_2Te_3 octahedron become shortened and lengthened, respectively, and an unpaired electron appears on the Te atoms bonded to Ag.

and Ag-doped Sb_2Te_3, we confirmed that both the performance and endurance are enhanced, suggesting that Ag-doped Sb_2Te_3 is a more suitable material for PCMs.

To identify the origin of the amelioration in the phase change properties of Sb_2Te_3 with Ag doping, the local structures of Sb_2Te_3 and Ag-doped Sb_2Te_3 were investigated in detail. Among the three vibration modes of Sb_2Te_3, E_g^2 (69 cm^{-1}), A_{1g}^1 (112 cm^{-1}), and A_{1g}^2 (166 cm^{-1}), the first is related to the in-plane phonon mode corresponding to the vibration of the Sb−Te bonds within two-dimensional Sb_2Te_3 plane, and the other two indicate the out-of-plane phonon vibrations involving the van der Waals interaction between Sb_2Te_3 layers.[50] Therefore, changes in the vibration modes after the Ag incorporation may provide information on whether the Ag dopant is located in the Sb_2Te_3 quintuple layer or in the van der Waals gap between the layers. If the dopant is placed inside the quintuple layer, the in-plane phonon vibration should be affected and a change in the E_g^2 mode should be observed. Otherwise, there should be observed changes in the A_{1g}^1 or A_{1g}^2 mode. As shown in Figure 4a, we observed a peak position shift in the E_g^2 mode, whereas no shift was observed in the A_{1g}^1 and A_{1g}^2 ones. Therefore, the Ag atom is assumed to be located inside the Sb_2Te_3 quintuple layer. The XRD data can provide additional information on the crystal structure change after the incorporation of Ag in Sb_2Te_3. The diffraction peaks of the (009) plane of Sb_2Te_3 and Ag-doped Sb_2Te_3 are compared in Figure 4b; the diffraction peak shifted to a lower angle after Ag incorporation. This implies that the incorporated atom is located in the Sb−Te plane, either in a substitutional or interstitial site. Additionally, the direction of the peak shift indicates a change in the lattice parameter related to the substitution of the dopant, with a dependence on its size. Because the atomic radius of Ag (160 pm) is larger than that of Sb (145 pm) and Te (140 pm),[22] the lattice constant of Sb_2Te_3 should increase after doping, and the diffraction peak

should consistently shift to a lower angle, according to Bragg's law ($n\lambda = d \sin \theta$).[51]

To confirm the substitution of the Ag dopant, the chemical bonding was investigated by acquiring the X-ray photoelectron spectroscopy (XPS) profiles of Sb 3d and Te 3d in Sb_2Te_3 and Ag-doped Sb_2Te_3 (Figure 4c,d, respectively). A peak shift to a lower binding energy was observed in both spectra, and no new peak appeared. Peak shifts in XPS are known to be caused by changes in the electronegativity of the elements because valence electrons are more attracted to the nucleus after bonding to an element with a lower electronegativity. Thus, the formation of a bond to an element with a lower electronegativity or the reduction of the bond to an element with a higher electronegativity causes a peak shift to lower binding energies. Because the electronegativities of Ag, Sb, and Te are 1.93, 2.05, and 2.1, respectively,[21] the peak shifts to lower binding energies in the Sb 3d and Te 3d spectra after Ag incorporation can be explained by the formation of Ag−Te bonds and reduction of the Sb−Te ones. This can be confirmed by the XPS Ag 3d spectrum. In fact, the Ag 3d peak of Ag-doped Sb_2Te_3 has a higher binding energy than that of bare Ag, consistent with the formation of Ag−Te bonds. Therefore, the formation of Ag−Te bonds and reduction of the Sb−Te ones support Ag substitution in the Sb site of the Sb−Te layer, possibly inducing reliable distortion in the Sb_2Te_3 lattice.

Using the experimental evidence of changes in the local structure of Ag-doped Sb_2Te_3, *ab initio* density functional theory (DFT) calculations were conducted to confirm the change in the hexagonal closed-packed Sb_2Te_3 crystal lattice. To find the location of the dopant, we calculated the formation energies of six different Ag-doped Sb_2Te_3 structures. Figure S6a shows all the dopant sites, which are two Te substitution, one Sb substitution, and three interstitial sites. The hexagonal symmetry of the quintuple layers guarantees that six different dopant sites are enough to be considered. We found that the

Ag substitution for an Sb atom forms the most stable Ag-doped Sb_2Te_3 structure shown in Figure S6b as confirmed by our experimental data. Figure S6c displays our calculated formation energies for the six different Ag-doped Sb_2Te_3 configurations.

To identify the changes in the local environment and chemical bonding caused by Ag incorporation, charge density difference (CDD) was evaluated for the Sb_2Te_3 and Ag-doped Sb_2Te_3 lattices (Figure 5a,b, respectively). The local environment of Sb_2Te_3 consists of six-coordinated Te, three-coordinated Te, and six-coordinated Sb (right panel of Figure 5a). The six-coordinated Te has six identical resonant-like bonds, whereas the three-coordinated Te has three identical covalent-like bonds to Sb atoms. Because the resonant-like bonds have on average 1 p-electron per bond, the bonds are relatively weaker and longer than the covalent-like bonds, which have in average 2 p-electrons per bond.[43] Particularly, because the formation of the covalent-like bond removes the unpaired electron of Te, there is no electron charge inside the van der Waals gap, and the three-coordinated Te locates at the outer surfaces of the Sb_2Te_3 quintuple layer. Consequently, the six-coordinated Sb has three long bonds with a length of 3.14 Å and three short bonds with a length of 3.00 Å resulting from Peierls-like instability. The bond angles in all local environments of Sb_2Te_3 are approximately 90°, indicating an octahedral atomic configuration.[52]

Ag incorporation brings new atomic configurations in the local Sb_2Te_3 environment (right panel of Figure 5b). First, the substituted Ag atom acquires a three-coordinated atomic configuration with three identical bonds to Te atoms with a bond length of 2.78 Å, implying much stronger bonds than the short Sb−Te bonds, locating the Ag atom closer to the middle Te atom layer with respect to the original Sb site. Considering the covalent radii of Ag (1.45 Å) and Te (1.38 Å),[53] the ionic contribution in the strong Ag−Te bond may be relevant. Additionally, the bond angle between Ag and Te was evaluated to be ~105°, implying the formation of a defective tetrahedral atomic configuration.[52] This local environment is similar to that of Ag_2Te, which consists of a Ag-centered tetrahedron and strong covalent bonds between Ag and Te. The strong bond may account for the increase in the thermal stability of Ag-doped Sb_2Te_3, similar to the effect reported for Ti-doped[19] and Sc-doped[4] Sb_2Te_3. The existence of the unpaired electron in the Te atom bonded with the Ag atom was observed similarly as in the case of Al-doped[17] and Ti-doped[19] Sb_2Te_3. Because Ag has a fully filled 4d orbital, surplus electrons can be induced by the chemical bond between Ag and Te. Thus, the number of unpaired electrons may be larger than in Ti-doped Sb_2Te_3 because Ti has only a partially filled 3d orbital. The unpaired electron can be beneficial in the formation of Te−Te homopolar bonds across the van der Waals gap during amorphization, consistent with the reduction in the RESET operation energy.[43] The incorporation of Ag also affects the Sb−Te bonds near Ag: in the six-coordinated Sb, one resonant-like bond weakens and another one strengthens, becoming a covalent-like bond by changing their lengths to 3.19 and 2.92 Å, respectively, from 3.14 Å. Therefore, the increase in the deviation of the chemical order caused by the bond modulation can strengthen the Peierls-like instability, as reported for Ag-doped GST[11] and consistent with the improvement in the SET operation characteristics. The number of bonds and bond length in the crystal lattices of Sb_2Te_3 and Ag-doped Sb_2Te_3 are summarized in Table 1.

Table 1. Bond Lengths of the Sb−Te Bond in Sb_2Te_3 and Ag−Te Bond in Ag-Doped Sb_2Te_3, Obtained by *Ab Initio* Calculations

parameter	Sb_2Te_3		Ag-doped Sb_2Te_3		
	short bond	long bond	short bond	long bond	Ag−Te bond
number of bond	3	3	3	3	3
length (Å)	3.00	3.14	3.00/2.92	3.14/3.19	2.78

For the room-temperature analysis on the bond lengths and bond angles, we evaluated the RDFs and angular distribution functions (ADFs) for Sb_2Te_3 and Ag-doped Sb_2Te_3 using *ab initio* MD simulations performed at room temperature (Figure S7). The changes in the bond nature in Sb_2Te_3 after the Ag incorporation are consistent with the DFT calculations for the frozen structures. Furthermore, the increase in distance between the Sb/Te atom and the 2nd or 3rd nearest neighboring atoms was confirmed, implying the formation of additional space inside the quintuple layer because of the substituted Ag position located in the middle Te atom layer. Such a change can be compensated by the formation of rigid Ag−Te bonds and facilitate the long-range order breaking, thereby decreasing the RESET operation energy. A more detailed discussion of this is presented in the Supporting Information.

In summary, the formation of a Ag-centered defective tetrahedron and the change in the crystal lattice of Sb_2Te_3 after the Ag incorporation were described through experimental results and *ab initio* calculations. Our study showed that both key factors for PRAM application, i.e., the increase in thermal stability and reduction in operation energy, could be achieved successfully. The evolutions of the resistance and crystal phase changes with annealing temperature verified the increase in crystallization temperature. At the same time, the decreases in the SET and RESET operation energies are also confirmed. Especially, RESET operation energy, which takes dominant proportion in operation energy, is reduced about 33% with Ag incorporation, and even three orders of magnitude lower than the already commercialized phase change material GST. We also showed that the Ag substitution in the Sb site of the Sb−Te quintuple layer generates new local environments and changes the Sb−Te bonding nature. A strong interaction between Ag and Te causes both an increase in Peierls distortion and reduction in distances between 1st nearest atoms, which make it possible to enhance thermal stability and operation energy. The interaction could be induced by the ionic contribution in the Ag−Te bond, which is caused by the fully filled d orbital in the valence shell of Ag. Moreover, this brings the unpaired electron of Te near the van der Waals gap, similar to the Ti-doped Sb_2Te_3 case. The number of electrons filling the d orbital may be vital to determining whether an element can enhance the phase change properties of Sb_2Te_3. Because the shielding of the nuclear charge depends on this number, the ionic bond contribution is also influenced. The generation of unpaired electrons and their number may also depend on the number of electrons filling the d orbital. Among the most suitable candidates (Ag, Cd, and Hg) for application to conventional memory devices, we chose the non-toxic Ag because it has the weakest shielding effect. In conclusion, this study suggests Ag-doped Sb_2Te_3 as a novel PCM because the electronic structure of the incorporated Ag can efficiently

increase the thermal stability and reduce the operation energy of PRAM devices.

ASSOCIATED CONTENT

Supporting Information

The Supporting Information is available free of charge at https://pubs.acs.org/doi/10.1021/acsami.0c05811.

$R-T$ curves of the Ag-doped Sb_2Te_3 film with various Ag contents; data retention properties of GST, Sb_2Te_3, and Ag-doped Sb_2Te_3; TEM images of Sb_2Te_3 and Ag-doped Sb_2Te_3; device operation characteristics of GST; resistance drift characteristics of Sb_2Te_3 and Ag-doped Sb_2Te_3; and *ab initio* calculation data of Ag-doped Sb_2Te_3 (PDF)

AUTHOR INFORMATION

Corresponding Author

Mann-Ho Cho − *Department of Physics and Atomic Scale Surface Science Center, Yonsei University, Seoul 03722, Republic of Korea;* orcid.org/0000-0002-5621-3676; Email: mh.cho@yonsei.ac.kr

Authors

Soobin Hwang − *Department of Physics and Atomic Scale Surface Science Center, Yonsei University, Seoul 03722, Republic of Korea*

Hanjin Park − *Department of Physics and Research Institute for Basic Sciences, Kyung Hee University, Seoul 02447, Republic of Korea*

Dasol Kim − *Department of Physics and Atomic Scale Surface Science Center, Yonsei University, Seoul 03722, Republic of Korea*

Hyeonwook Lim − *Department of Physics and Atomic Scale Surface Science Center, Yonsei University, Seoul 03722, Republic of Korea*

Changwoo Lee − *Department of Physics and Atomic Scale Surface Science Center, Yonsei University, Seoul 03722, Republic of Korea*

Jeong Hwa Han − *Department of Physics and Atomic Scale Surface Science Center, Yonsei University, Seoul 03722, Republic of Korea*

Young-Kyun Kwon − *Department of Physics and Research Institute for Basic Sciences, Kyung Hee University, Seoul 02447, Republic of Korea;* orcid.org/0000-0001-6027-8408

Complete contact information is available at: https://pubs.acs.org/10.1021/acsami.0c05811

Notes

The authors declare no competing financial interest.

ACKNOWLEDGMENTS

REFERENCES

(1) *IEEE Solid-State Circuits Magazine*; IEEE, 2016, 8, 1−8.

(2) Burr, G. W.; Kurdi, B. N.; Scott, J. C.; Lam, C. H.; Gopalakrishnan, K.; Shenoy, R. S. Overview of Candidate Device Technologies for Storage-Class Memory. *IBM J. Res. Dev.* **2008**, *52*, 449−464.

(3) Simpson, R. E.; Krbal, M.; Fons, P.; Kolobov, A. V.; Tominaga, J.; Uruga, T.; Tanida, H. Toward the Ultimate Limit of Phase Change in $Ge_2Sb_2Te_5$. *Nano Lett.* **2010**, *10*, 414−419.

(4) Rao, F.; Ding, K.; Zhou, Y.; Zheng, Y.; Xia, M.; Lv, S.; Song, Z.; Feng, S.; Ronneberger, I.; Mazzarello, R.; Zhang, W.; Ma, E. Reducing the Stochasticity of Crystal Nucleation to Enable Subnanosecond Memory Writing. *Science* **2017**, *358*, 1423−1427.

(5) Newsroom, I. *Introducing Intel Optane Technology—Bringing 3D XPoint Memory to Storage and Memory Products*; https://newsroom.intel.com/press-kits/introducing-intel-optane-technology-bringing-3d-xpoint-memory-to-storage-and-memory-products/, 2015.

(6) Kolobov, A. V.; Fons, P.; Frenkel, A. I.; Ankudinov, A. L.; Tominaga, J.; Uruga, T. Understanding the Phase-Change Mechanism of Rewritable Optical Media. *Nat. Mater.* **2004**, *3*, 703−708.

(7) Cho, E.; Youn, Y.; Han, S. Enhanced Amorphous Stability of Carbon-Doped $Ge_2Sb_2Te_5$: Ab Initio investigation. *Appl. Phys. Lett.* **2011**, *99*, 183501−183504.

(8) Zhou, X.; Wu, L.; Song, Z.; Rao, F.; Zhu, M.; Peng, C.; Yao, D.; Song, S.; Liu, B.; Feng, S. Carbon-Doped $Ge_2Sb_2Te_5$ phase Change Material: a Candidate for High-Density Phase Change Memory Application. *Appl. Phys. Lett.* **2012**, *101*, 142104−142105.

(9) Jeong, T. H.; Kim, M. R.; Seo, H.; Park, J. W.; Yeon, C. Crystal Structure and Microstructure of Nitrogen-Doped $Ge_2Sb_2Te_5$ Thin Film. *Jpn. J. Appl. Phys.* **2000**, *39*, 2775−2779.

(10) Jang, M. H.; Park, S. J.; Ahn, M.; Jeong, K. S.; Park, S. J.; Cho, M.-H.; Song, J. Y.; Jeong, H. Ultrafast Phase Change and Long Durability of BN-Incorporated GeSbTe. *J. Mater. Chem. C* **2015**, *3*, 1707−1715.

(11) Han, J. H.; Jeong, K.-S.; Ahn, M.; Lim, D.-H.; Yang, W. J.; Park, S. J.; Cho, M.-H. Modulation of Phase Change Characteristics in Ag-Incorporated $Ge_2Sb_2Te_5$ Owing to Changes in Structural Distortion and Bond Strength. *J. Mater. Chem. C* **2017**, *5*, 3973−3982.

(12) Li, X.-B.; Chen, N.-K.; Wang, X.-P.; Sun, H.-B. Phase-Change Superlattice Materials Toward Low Power Consumption and High Density Data Storage: Microscopic Picture, Working Principles, and Optimization. *Adv. Funct. Mater.* **2018**, *28*, 1803380.

(13) Liu, B.; Song, Z.; Feng, S.; Chen, B. Characteristics of Chalcogenide Nonvolatile Memory Nano-Cell-Element Based on Sb_2Te_3 Material. *Microelectron. Eng.* **2005**, *82*, 168−174.

(14) Kim, M.-Y.; Oh, T.-S. Crystallization Behavior and Thermoelectric Characteristics of the Electrodeposited Sb_2Te_3 Thin Films. *Thin Solid Films* **2010**, *518*, 6550−6553.

(15) Yin, Y.; Sone, H.; Hosaka, S. Characterization of Nitrogen-Doped Sb_2Te_3 Films and Their Application to Phase-Change Memory. *J. Appl. Phys.* **2007**, *102*, 064503−064506.

(16) Yin, Y.; Morioka, S.; Kozaki, S.; Satoh, R.; Hosaka, S. Oxygen-Doped Sb_2Te_3 for High-Performance Phase-Change Memory. *Appl. Surf. Sci.* **2015**, *349*, 230−234.

(17) Xia, M.; Ding, K.; Rao, F.; Li, X.; Wu, L.; Song, Z. Aluminum-Centered Tetrahedron-Octahedron Transition in Advancing Al-Sb-Te Phase Change Properties. *Sci. Rep.* **2015**, *5*, 8548.

(18) Ji, X.; Wu, L.; Cao, L.; Zhu, M.; Rao, F.; Zheng, Y.; Zhou, W.; Song, Z.; Feng, S. Vanadium Doped Sb_2Te_3 material with Modified Crystallization Mechanism for Phase-Change Memory Application. *Appl. Phys. Lett.* **2015**, *106*, 243103−243106.

(19) Zhu, M.; Xia, M.; Rao, F.; Li, X.; Wu, L.; Ji, X.; Lv, S.; Song, Z.; Feng, S.; Sun, H.; Zhang, S. One Order of Magnitude Faster Phase Change at Reduced Power in Ti-Sb-Te. *Nat. Commun.* **2014**, *5*, 1.

(20) Lloyd, D. R. On the Lanthanide and "Scandinide" Contractions. *J. Chem. Educ.* **1986**, *63*, 502−502.

(21) Pauling, L. *The Nature of the Chemical Bond and the Sturucture of Molecules and Crystals*; Cornell University Press:Ithaca, New York, 1939.

(22) Slater, J. C. Atomic Radii in Crystals. *J. Chem. Phys.* **1964**, *41*, 3199−3204.

(23) Zhang, Y.; Li, Y.; Ma, Y.; Li, Y.; Li, G.; Shao, X.; Wang, H.; Cui, T.; Wang, X.; Zhu, P. Electronic Topological Transition in Ag_2Te at High-Pressure. *Sci. Rep.* **2015**, *5*, 14681.

(24) Fragkos, S.; Sant, R.; Alvarez, C.; Bosak, A.; Tsipas, P.; Tsoutsou, D.; Okuno, H.; Renaud, G.; Dimoulas, A. Room Temperature Commensurate Charge Density Wave in Epitaxial Strained $TiTe_2$ Multilayer Films. *Adv. Mater. Interfaces* **2019**, *6*, 1801850−1801839.

(25) Zhu, M.; Song, W.; Konze, P. M.; Li, T.; Gault, B.; Chen, X.; Shen, J.; Lv, S.; Song, Z.; Wuttig, M.; Dronskowski, R. Direct Atomic Insight Into the Role of Dopants in Phase-Change Materials. *Nat. Commun.* **2019**, *10*, 1−10.

(26) Arun, P.; Tyagi, P.; Vedeshwar, A. G.; Kumar Paliwal, V. Ageing Effect of Sb_2Te_3 Thin Films. *Phys. B* **2001**, *307*, 105−110.

(27) Sebastian, A.; Krebs, D.; Le Gallo, M.; Pozidis, H.; Eleftheriou, E. A Collective Relaxation Model for Resistance Drift in Phase Change Memory Cells. In *2015 IEEE International Reliability Physics Symposium*; IEEE, 2015.

(28) Kohn, W.; Sham, L. J. Self-Consistent Equations Including Exchange and Correlation Effects. *Phys. Rev.* **1965**, *140*, A1133−A1138.

(29) Kresse, G.; Joubert, D. From Ultrasoft Pseudopotentials to the Projector Augmented-Wave Method. *Phys. Rev. B* **1999**, *59*, 1758−1775.

(30) Perdew, J. P.; Zunger, A. Self-Interaction Correction to Density Functional Approximation for Many Electron Systems. *Phys. Rev. B* **1981**, *23*, 5048.

(31) Kresse, G.; Hafner, J. *Ab Initio* Molecular Dynamics for Liquid Metals. *Phys. Rev. B* **1993**, *47*, 558−561.

(32) Perdew, J. P.; Burke, K.; Ernzerhof, M. Generalized Gradient Approximation Made Simple. *Phys. Rev. Lett.* **1996**, *77*, 3865−3868.

(33) Grimme, S. Semiempirical GGA-Type Density Functional Constructed with a Long-Range Dispersion Correction. *J. Comput. Chem.* **2006**, *27*, 1787−1799.

(34) Nosé, S. A Molecular Dynamics Method for Simulations in the Canonical Ensemble. *Mol. Phys.* **2006**, *52*, 255−268.

(35) Hoover, W. G. Canonical Dynamics: Equilibrium Phase-Space Distributions. *Phys. Rev. A* **1985**, *31*, 1695−1697.

(36) Allen, M. P.; Tildesley, D. J. *Computer Simulation of Liquids*; Oxford Univ., 1989.

(37) Rapaport, D. C.; Rapaport, D. C. R. *The Art of Molecular Dynamics Simulation*; Cambridge university press, Cambridge, United Kingdom, 2004.

(38) Park, S. J.; Park, H.; Jang, M. H.; Ahn, M.; Yang, W. J.; Han, J. H.; Jeong, H. S.; Kim, C.-W.; Kwon, Y.-K.; Cho, M.-H. Laser Irradiation-Induced Modification of the Amorphous Phase in GeTe Films: the Role of Intermediate Ge-Te Bonding in the Crystallization Mechanism. *J. Mater. Chem. C* **2015**, *3*, 9393−9402.

(39) Lawal, A.; Shaari, A.; Ahmed, R.; Jarkoni, N. Sb_2Te_3 Crystal a Potential Absorber Material for Broadband Photodetector: a First-Principles Study. *Results Phys.* **2017**, *7*, 2302−2310.

(40) Zhang, H. B.; Yu, H. L.; Yang, G. W. Experimental Evidence of the Nanoscaled Topological Metallic Surface State of Bi_2Te_3 and Sb_2Te_3 films. *EPL* **2011**, *95*, 56002−56007.

(41) Kao, K.-F.; Lee, C.-M.; Chen, M.-J.; Tsai, M.-J.; Chin, T.-S. $Ga_2Te_3Sb_5$-A Candidate for Fast and Ultralong Retention Phase-Change Memory. *Adv. Mater.* **2009**, *21*, 1695−1699.

(42) Richter, W.; Becker, C. R. A Raman and Far-Infrared Investigation of Phonons in the Rhombohedral V_2−VI_3 Compounds Bi_2Te_3, Bi_2Se_3, Sb_2Te_3 and $Bi_2(Te_{1−x}Se_x)_3$ $(0 < x < 1)$, $(Bi_{1−y}Sb_y)_2Te_3$ $(0 < y < 1)$. *Phys. Status Solidi B* **1977**, *84*, 619−628.

(43) Zheng, Y.; Xia, M.; Cheng, Y.; Rao, F.; Ding, K.; Liu, W.; Jia, Y.; Song, Z.; Feng, S. Direct Observation of Metastable Face-Centered Cubic Sb_2Te_3 Crystal. *Nano Res.* **2016**, *9*, 3453−3462.

(44) Wu, H.-J.; Chen, S.-W. Phase Equilibria of Ag-Sb-Te Thermoelectric Materials. *Acta Mater.* **2011**, *59*, 6463−6472.

(45) Hatayama, S.; Sutou, Y.; Shindo, S.; Saito, Y.; Song, Y.-H.; Ando, D.; Koike, J. Inverse Resistance Change $Cr_2Ge_2Te_6$-Based PCRAM Enabling Ultralow-Energy Amorphization. *ACS Appl. Mater. Interfaces* **2018**, *10*, 2725−2734.

(46) Mori, S.; Hatayama, S.; Shuang, Y.; Ando, D.; Sutou, Y. Reversible Displacive Transformation in MnTe Polymorphic Semiconductor. *Nat. Commun.* **2020**, *11*, 1−8.

(47) Liu, B.; Liu, W.; Li, Z.; Li, K.; Wu, L.; Zhou, J.; Song, Z.; Sun, Z. Y-Doped Sb_2Te_3 Phase-Change Materials: Toward a Universal Memory. *ACS Appl. Mater. Interfaces* **2020**, *12*, 20672−20679.

(48) Shang, F.; Zhai, J.; Song, S.; Song, Z.; Wang, C. Improved Performance of Phase Change Memory Cell with Strontium Titanate and Barium Titanate Buffer Layer. *Jpn. J. Appl. Phys.* **2010**, *49*, 094202−094206.

(49) Zhu, M.; Wu, L.; Rao, F.; Song, Z.; Ren, K.; Ji, X.; Song, S.; Yao, D.; Feng, S. Uniform Ti-Doped Sb_2Te_3 materials for High-Speed Phase Change Memory Applications. *Appl. Phys. Lett.* **2014**, *104*, 053119.

(50) Sosso, G. C.; Caravati, S.; Bernasconi, M. Vibrational Properties of Crystalline Sb_2Te_3 From First Principles. *J. Phys.: Condens. Matter* **2009**, *21*, 095410−095417.

(51) Wang, Q.; Liu, B.; Xia, Y.; Zheng, Y.; Huo, R.; Zhu, M.; Song, S.; Lv, S.; Cheng, Y.; Song, Z.; Feng, S. Characterization of Cr-Doped Sb_2Te_3 films and Their Application to Phase-Change Memory. *Phys. Stat. Sol. (RRL)* **2015**, *9*, 470−474.

(52) Caravati, S.; Bernasconi, M.; Parrinello, M. First-Principles Study of Liquid and Amorphous Sb_2Te_3. *Phys. Rev. B* **2010**, *81*, 014201.

(53) Cordero, B.; Gómez, V.; Platero-Prats, A. E.; Revés, M.; Echeverría, J.; Cremades, E.; Barragán, F.; Alvarez, S. Covalent Radii Revisited. *Dalton Trans.* **2008**, *0*, 2832−2838.